ADVANCED ELECTRONIC MATERIALS
www.advelectronicmat.de

Simultaneous Enhancement of Actuation Strain and Mechanical Strength of Nanoporous Ni–Mn Actuators

Chuan Cheng, Lukas Lührs, and Tobias Krekeler*

Metallic electrochemical actuators convert electrical energy into mechanical energy via charge-induced strain at the nanoporous metal/electrolyte interface. To enhance the actuation amplitude, a general choice is to increase the electrode surface area to elevate the charge capacity. However, a large surface area is detrimental to the actuation stability and mechanical strength of the actuator, such as irreversible volume shrinkage due to surface coarsening. Here, this critical issue can be mitigated by introducing a secondary actuation metal (Mn) into the network of a primary actuation metal (Ni). A nanoporous Ni–Mn actuator is synthesized by chemical dealloying with a controllable Mn content by adjusting dealloying conditions. Mn enriched nanowires are entangled with much larger sized Ni nanoligaments throughout the whole nanoporous network. Mn contributes a two-electron-transfer redox of $Mn(OH)_2/MnOOH/MnO_2$, which induces reversible volume change via H^+ intercalation/deintercalation. It is more efficient for strain generation than a one-electron-transfer redox of $Ni(OH)_2/NiOOH$ in the host. A recorded high reversible strain of 1.94% is obtained. Simultaneously, the mechanical strength of the actuator exponentially increases with the relative density due to the introduction of the secondary actuation metal.

1. Introduction

Electrochemical actuation materials convert electrical energy into mechanical energy via charge-induced strain effect at the nanoporous structured electrode/electrolyte interface during charge–discharge processes.[1] They have promising applications in micro-electromechanical systems for bio-inspired functions, that work in either wet (liquid electrolytes) or dry (solid electrolytes) environments, under low operating voltages ≈1 V which is ≈3 orders less than commercialized piezoelectric actuators.[1d,2] Different from electric motors that are composed of complex wheels and gears, an electrochemical actuator is usually a single piece of material, which enable it to be miniaturized and suitable for tasks that are difficult or impossible to achieve by motors, such as artificial muscles,[3] micro-fluid systems,[4] and electromechanical robots.[5] These actuation materials take advantage of the high surface-area-to-volume-ratio of nanoporous structures and transform charge-induced interatomic local strain into macroscopic volume change of the whole electrode,[1d,6] which can even be observed with the naked eye,[7] or lift a weight that was hundreds of times heavier than the actuator itself.[1b,5]

Many immerging actuators are based on soft materials for flexible applications,[8] such as carbon nanotube/graphene sheets/yarns,[1a,2e,9] conducting polymers,[4,10] 2D materials,[1b] and ionic polymer-metal composites;[11] while rigid and 3D bulk actuators, similar to those piezoelectric competitors, are rare and mainly nanoporous metal-based electrochemical actuators, because of their high strength and stiffness.[6,12] In the past two decades, researchers have spent plenty of efforts to face critical challenges of metallic actuators to enhance the actuation strain from ≈0.1% to ≈1%,[1d,6,7b,13] elevate charge–strain response rate against sluggish ion diffusion,[12b,14] increase mechanical strength and stability against coarsening of metallic nanoporous structures,[15] and replace precious noble metals with low-cost transition-metals.[7a,13c,16]

However, there is a dead-lock problem that has not been solved. On the one hand, a high specific surface area of the metallic actuator is required to achieve large actuation strain, because the charge-induced strain is proportional to the specific capacity, and the high surface area is a pre-condition to store more charges at the electrode/electrolyte interface either by non-faradaic capacitance or by faradaic pseudocapacitance.[16d,17] On the other hand, high specific surface area leads to mechanical weakness of the actuator, such as irreversible volume shrinkage driven by the high surface-free-energy and low mechanical strength to bear and output the actuation load.[6,18] Therefore, even though the simultaneously high specific surface area and mechanical stability were regarded as critical for metallic actuators to achieve competitive performances,[1d] these two factors are difficult to coexist.

Dr. C. Cheng, Dr. L. Lührs
Institute of Materials Physics and Technology
Hamburg University of Technology
21073 Hamburg, Germany
E-mail: Chuan.Cheng@warwick.ac.uk
Dr. C. Cheng
Warwick Manufacturing Group
University of Warwick
Coventry CV4 7AL, UK
Dr. T. Krekeler
Electron Microscopy Unit
Hamburg University of Technology
21073 Hamburg, Germany
The ORCID identification number(s) for the author(s) of this article can be found under https://doi.org/10.1002/aelm.202100381.

DOI: 10.1002/aelm.202100381

This article demonstrates a different strategy to solve the above problem which can enhance both actuation strain and mechanical strength of metallic actuators at the same time. The actuation strain is enhanced by a secondary and more effective (higher capacitance) actuation metal in the nanoporous network of a primary actuation metal, while the mechanical strength is increased because the secondary actuation metal increases the relative density of the porous structure. Here, we select transition-metal Ni–Mn composite as an example, which is synthesized by selectively etching of Mn from $Ni_{30}Mn_{70}$ precursor. Due to the parting limit (dealloying threshold),[19] Mn is not completely etched away and the residual Mn content can be controlled by dealloying conditions; importantly, residual Mn is homogeneously integrated and evenly distributed on a 3D interconnected Ni network realized by chemical dealloying.

Mn oxides/hydroxides grow on the metal surface during charge–discharge, which exhibit super faradaic pseudocapacitance (e.g., 1380 F g^{-1} for MnO_2),[20] and it is very promising to generate high actuation strain. The primary actuation metal Ni experiences $Ni(OH)_2$/NiOOH redox reactions on the surface and also induces strain due to lattice mismatch among surface atoms.[21] 3D interconnected metal skeleton exists beneath the metal oxides/hydroxides layers, which provides a highly electric conductive network to facilitate pseudocapacitive charge storage/release—important for the fast charge–strain response.[20a,21a] Thus, this article reports a high-performance metallic muscle designed from a new strategy to simultaneously enhance actuation strain and mechanical strength, combined with a low-cost fabrication method.

2. Results and Discussion

Nanoporous Ni–Mn metal was synthesized by selectively etching less noble metal Mn from a $Ni_{30}Mn_{70}$ precursor within a weak acidic solution of $(NH_4)_2SO_4$.[16b] The precursor was cast from pure Ni and Mn metals by an induction furnace in the Ar atmosphere. During dealloying, atoms of the more noble metal (Ni) aggregate into ligaments through a phase separation process and finally form a bi-continuous nanoporous structure.[19,22] Due to the parting limit of dealloying,[19] Mn was not completely removed and the residual Mn content was controlled by dealloying conditions, including acid concentration, temperature, and dealloying time (see later in Section 2.3).

2.1. Electron Microscopy Characterization of Nanoporous Ni–Mn

Figure 1a shows a typical as-dealloyed nanoporous metal that has mm-scales in three dimensions. A scanning transmission electron microscopy (STEM) image of Figure 1b reveals a nanoporous structure inside the sample. Figure 1c notices a circular area for selected-area-diffraction (SEAD). The SEAD pattern in Figure 1d indicates a single-crystal within the selected area that contains hundreds of ligaments. The SEAD pattern shows characteristic features of an fcc structured crystal with the electron beam along the [011] zone axis.[23] From the measurement of the $g_{11\bar{1}}$ vector in the SEAD pattern, $d_{(11\bar{1})} = 2.05$ Å is obtained, which is consistent with the d-spacing measured from the

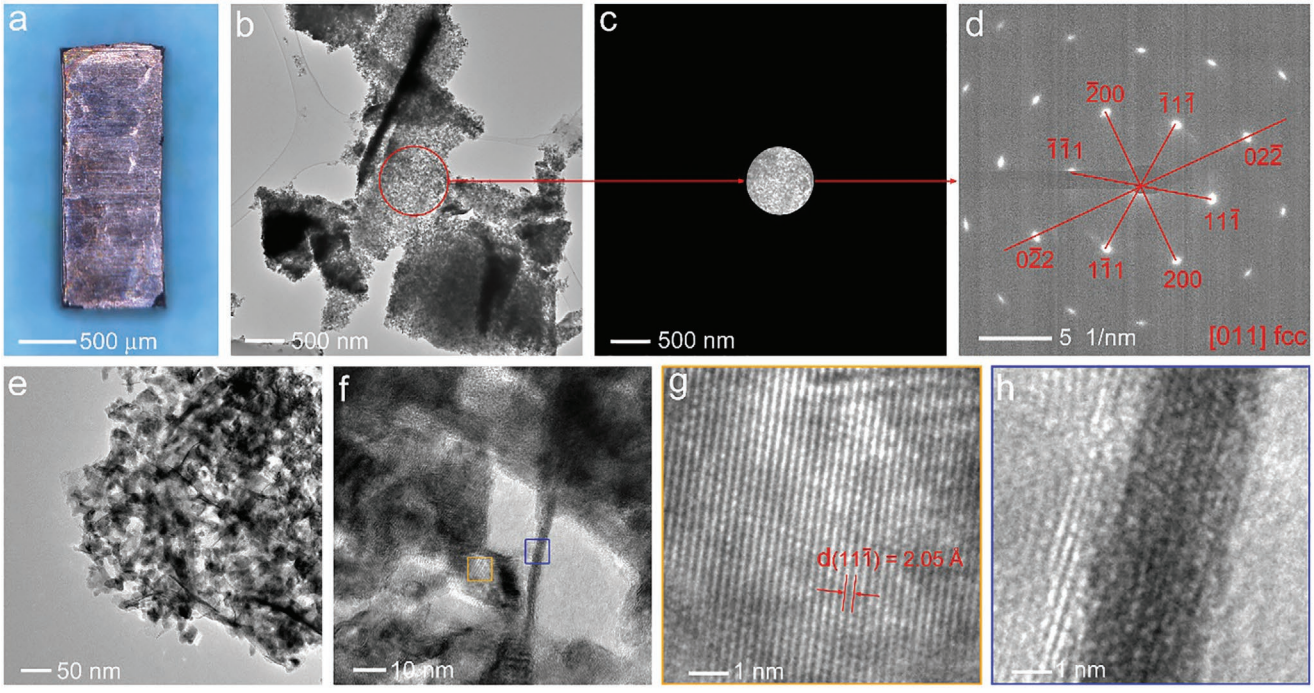

Figure 1. Characterization of as-dealloyed nanoporous Ni–Mn metal. a) Optical image of a bulk as-dealloyed sample. b) STEM image of the sample reveals nanoporous structures. c) A selected area (≈860 nm in diameter) for electron diffraction. d) The electron diffraction pattern indicates a single and fcc structured crystal in the selected area, with the electron beam along the [011] zone axis. e,f) Enlarged STEM images of the nanoporous metal which consists of larger-sized ligaments and smaller-sized wire-like structures. g) An enlarged STEM image captured on a ligament shows a d-spacing of 2.05 Å. h) An enlarged STEM image captured on a wire shows no obvious atomic arrangement.

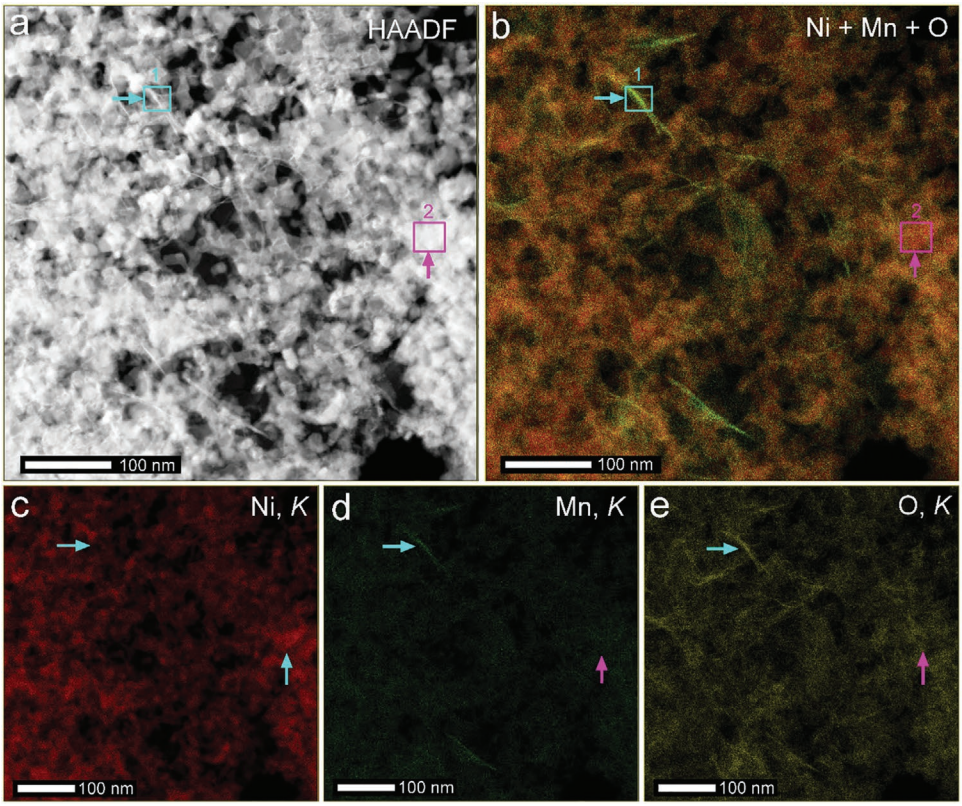

Figure 2. Element distribution in the nanoporous Ni–Mn metal. a) High-angle annular dark-field image of the nanoporous metal showing wire-like structures entangled in the nanoporous network. b) STEM-EDX element mapping of (a) with a mixed distribution of Ni (red), Mn (green), and O (yellow). c–e) Individual element mapping of Ni, Mn, and O, respectively, corresponding to (b). Cyan arrows notice the location of a wire which is relatively rich in Mn and O content. Pink arrows notice the location of a ligament that is relatively rich in Ni content.

STEM image that captured on a ligament (Figure 1g) and corresponds to the $(11\overline{1})$ plane of Ni metal.

Figure 1e,f show that the nanoporous structure is composed of interconnected ligaments (diameter ≈ 18 nm). Much smaller sized wires (diameter ≈ 4 nm) are entangled with the ligament network. Different from the ligament which shows an ordered atomic arrangement corresponding to Ni (Figure 1g), no obvious atomic arrangement is observed from the wire (Figure 1h). Because the SEAD pattern was generated from an area that contained hundreds of ligaments plus entangled wires, it indicates that the wires may either share the same crystal structure as ligaments or otherwise, amorphous.

Energy-dispersive X-ray spectroscopy (EDX) element mapping of the nanoporous metal was then conducted to further analyze the difference between ligaments and wires. **Figure 2**a shows a high-angle annular dark-field image of the nanoporous metal in which the wire-like structures can be more obviously observed. Cyan and pink arrows are used to trace a wire location and a ligament location, respectively. Figure 2b shows an overlapped element mapping corresponding to Figure 1a, which includes elements of Ni (red), Mn (green), and O (yellow); while individual element mappings are shown in Figure 2c–e. From the color contrast, the wire is relatively rich in Mn and O content, while the ligament is relatively rich in Ni content.

Quantitatively, the wire region noticed by rectangle #1 has an element ratio of Ni:Mn:O = 43.8:9.0:47.2 at%; while the ligament region noticed by rectangle #2 has an element ratio of Ni:Mn:O = 81.6:3.2:15.2 at%. The wire region has three times as many Mn and O content as the ligament region. The much higher O content on the Mn-enriched wire indicates that Mn has been oxidized into a higher valence state than Ni, so that MnO_x contains more oxygen than NiO_x per metal atom.[20a,24] The overall element ratio in Figure 2b is Ni:Mn:O = 70.0:3.7:26.3 at%. If only metal atoms are considered, the residual Mn content within the nanoporous metal is 5.0 at%. EDX is used to determine element distribution and content on the surface of ligaments/wires, rather than other methods such as inductively coupled plasma optical emission spectrometry for the average element content of the whole sample, because it is the surface atoms rather than atoms deeply beneath the surface will participate in the electrochemical reactions and contribute to the actuation.

From STEM characterizations in Figures 1,2, the as-dealloyed nanoporous metal is composed of interconnected Ni ligaments that are entangled with smaller-sized and Mn enriched wires. This heterogeneous distribution of elements is further confirmed after annealing because the high temperature facilitates surface coarsening of nano-structures.

The as-dealloyed nanoporous metal was annealed in a vacuum ($<10^{-5}$ torr) at 800 °C for 10 min. During this process, the original wires shrank into nanodots (60 to 100 nm) to reduce surface free energy; at the same time, the ligament

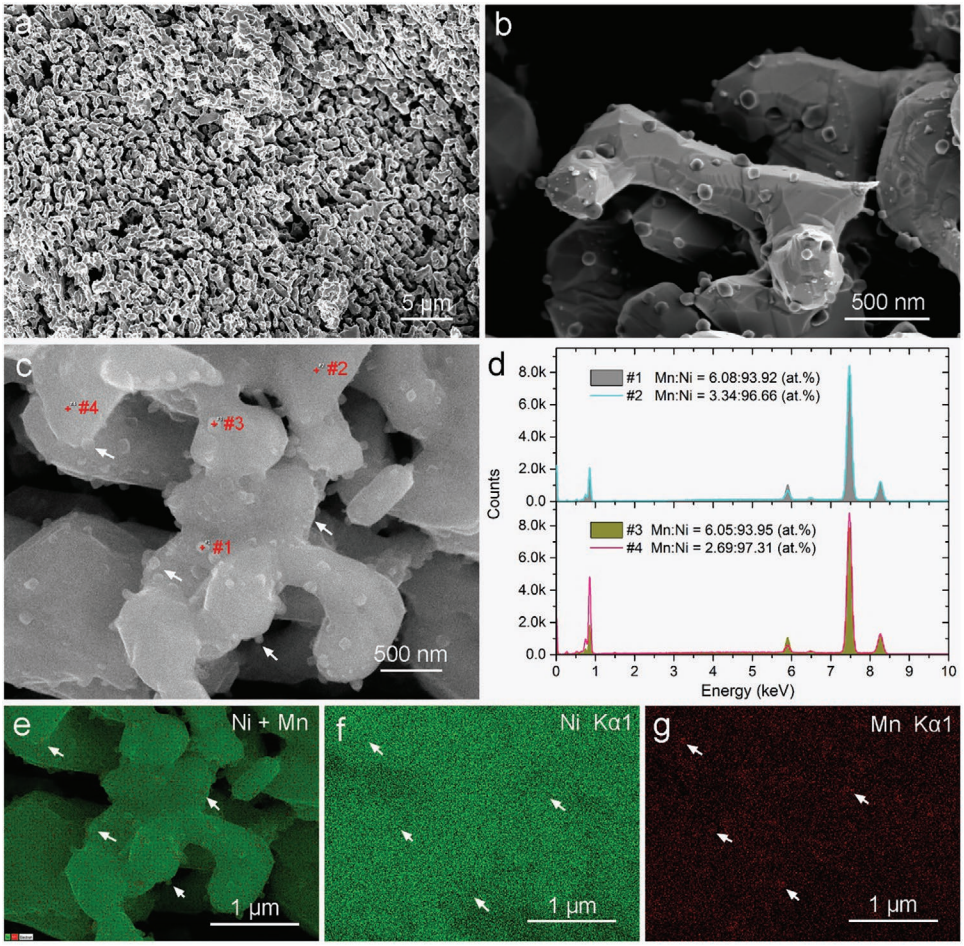

Figure 3. SEM characterization of annealed nanoporous Ni–Mn metal. a) A bi-continuous porous structure obtained after annealing in a vacuum (<10^{-5} torr) at 800 °C for 10 min. b) An enlarged image shows nanodots formed on ligaments. c,d) EDX point spectra on nanodots (#1 and #3) and ligaments (#2 and #4) as noticed in (c). e–g) EDX element mapping corresponding to (c), with Ni showing in green color and Mn showing in red color.

diameter grew from ≈18 to ≈350 nm, as shown in **Figure 3**a,b. The nanodots are evenly distributed on the surface of ligaments throughout the whole porous network (Figure 3b), while the ligament structure turns to be a bi-continuous structure, which was typically found in dealloyed nanoporous gold.[13b]

According to SEM-EDX point analysis shown in Figure 3c,d, the nanodots contain one time more Mn element than the ligaments (i.e., 6.1 at% vs 3.0 at%), which follows a similar trend shown in the as-dealloyed nanoporous metal (Figure 2). The unique phenomenon of nanodot formation indicates phase separation between Ni ligaments and oxidized Mn dots. As noticed by the arrows in Figure 3e–g, Mn enriched nanodots can also be observed from SEM-EDX mapping through the porous structure.

2.2. In Situ Electrochemical Actuation of Nanoporous Ni–Mn

Electrochemical actuation of as-dealloyed nanoporous Ni–Mn metal was measured by in situ dilatometry in an electrochemical cell. As illustrated in **Figure 4**a, a bulk nanoporous metal was immersed in an electrolyte and electrically connected to the working electrode (WE) of a potentiostat via a gold substrate and a gold wire. The top surface of the sample was contacted with the pushrod of a dilatometer under constant compressive pressure of ≈0.2 MPa. When charge-induced volume change happens in the nanoporous metal, the pushrod senses the vertical displacement of the sample. After that, the uniaxial strain, $\varepsilon = \Delta L/L_0$ is calculated, where L_0 is the original length of the sample and ΔL is the length change.

Figure 4 investigates two nanoporous Ni–Mn metals with different relative densities compared with solid Ni, that is, $\varphi = 40.0\%$ and $\varphi = 33.3\%$. The relative density equals to the density of the nanoporous metal divided by the density of solid Ni. A higher relative density corresponds to a higher Mn content within the sample (see later in Figure 7f). It is because Mn is more active than Ni, that is, the standard electrode potential of $E^0_{Mn^{2+}/Mn} = -1.18$ V while $E^0_{Ni^{2+}/Ni} = -0.25$ V, Mn will be selectively etched from the alloy precursor, while Ni will be intact before complete removing of Mn. However, due to the parting limit of the dealloying process,[19] Mn cannot be completely removed. Therefore, the increase of relative density is attributed to the increase in residual Mn content. By comparing the actuation behavior of samples

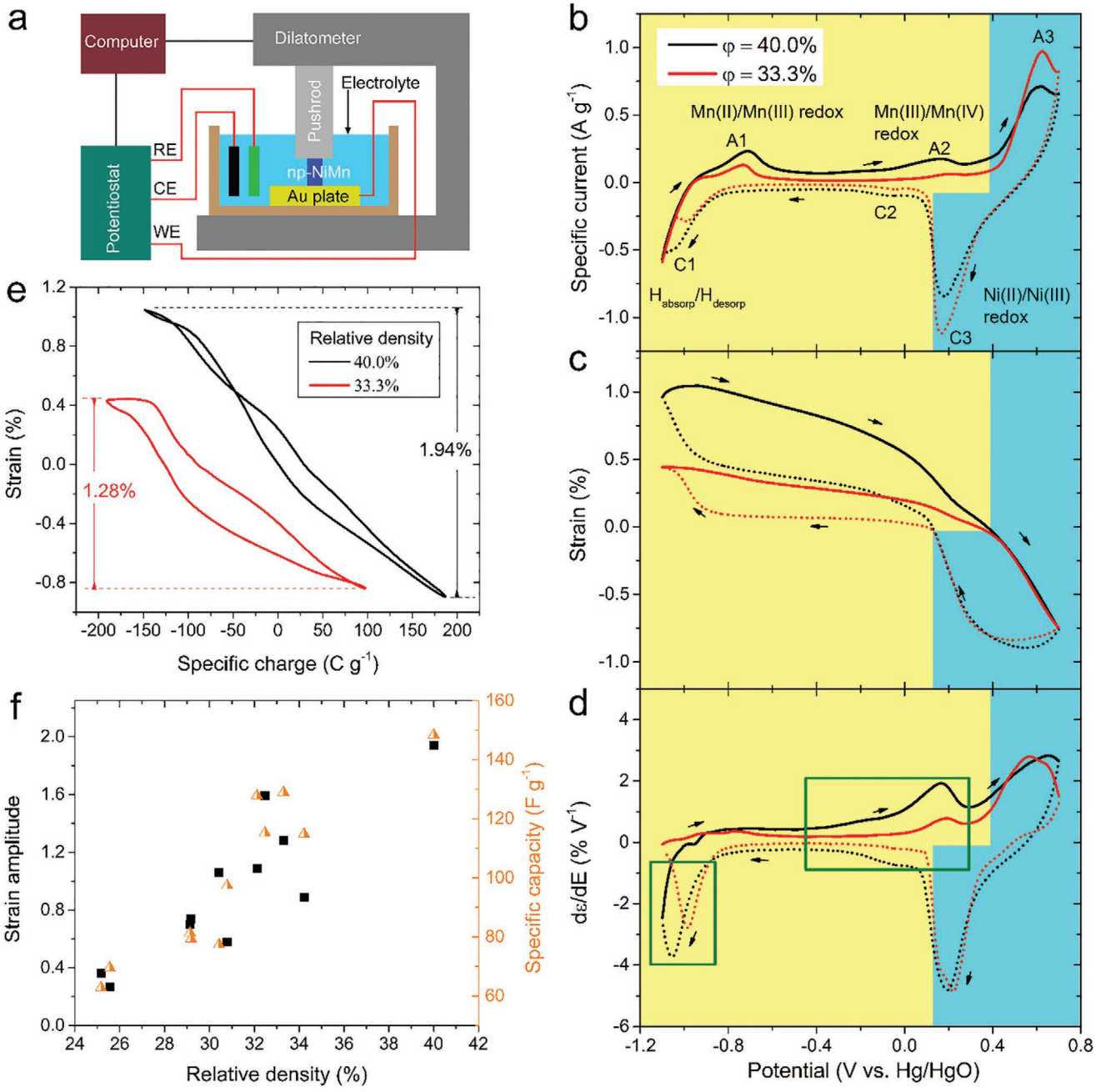

Figure 4. Electrochemical actuation of as-dealloyed nanoporous Ni–Mn with different relative densities, φ. a) Illustration of an experimental setup for in situ measurement. b) Cyclic voltammetry of nanoporous metals in 1 M NaOH electrolyte at 1 mV s^{-1} scan rate. c) Actuation strain as a function of electrode potential. d) Strain-potential coefficient ($d\varepsilon/dE$) as a function of potential. For a clear illustration, the coefficient of the anodic scan (solid curve) is multiplied by –1. e) Reversible actuation strain as a function of specific charge. f) Actuation strain amplitude as a function of relative density (left axis), and specific capacity as a function of relative density (right axis).

with different relative densities, the actuation contribution of Mn can be disclosed.

Cyclic voltammetry (CV) of the two samples was conducted in 1 M NaOH electrolyte at 1 mV s^{-1} scan rate. In Figure 4b, both samples are dominated by electrochemical signals of the Ni component. Specifically, the cathode peak C1 and anodic peak A1 are due to hydrogen absorption and then desorption into/from Ni,[25] which leads to volume expansion and then contraction. These volume changes have been reflected by the increase and then decrease of the actuation strain, as shown in Figure 4c. Ni oxidation happens around the anodic peak A1, that is, Ni → α-Ni(OH)$_2$,[25a] which induces volume expansion and counteracts some part of the volume contraction induced by hydrogen desorption. In the middle of the CV, the flat current region corresponds to the electrochemical double-layer, which induces a linear change of the actuation strain,

as shown in the corresponding region in Figure 4c. During the positive scanning, α-$Ni(OH)_2$ transforms to a more stable phase of β-$Ni(OH)_2$.[26] The anodic peak A3 and cathodic peak C3 are attributed to the redox reaction of β-$Ni(OH)_2 + OH^- \leftrightarrow \beta$-$NiOOH + H_2O + e^-$. The lattice mismatching between β-NiOOH and β-$Ni(OH)_2$ results in volume contraction in the forward direction and expansion in the backward direction.[27] This redox reaction induces similar strain amplitude for both samples, as shown in the cyan region of Figure 4c. Because of the above series of reactions, both samples experience a continuous volume contraction during the positive scanning, which is recovered during the negative scanning (Figure 4c).

The electrochemical contribution of Mn is reflected by the difference between $\varphi = 40.0\%$ (black) and $\varphi = 33.3\%$ (red) in Figure 4b. Within an alkaline electrolyte, $Mn(OH)_2$ is formed on the Mn surface before testing, or at an electrode potential (–1.66V vs Hg/HgO)[28] that is below the present CV range. During positive scanning, $Mn(OH)_2$ is first oxidized to a transitional state:[21b,29] $Mn(OH)_2 + OH^- \rightarrow MnOOH + H_2O + e^-$, and then further oxidized to MnO_2 at the anodic peak A2:[29,30] $MnOOH + OH^- \rightarrow MnO_2 + H_2O + e^-$. Both reactions are accompanied by H^+ deintercalation from Mn compounds which lead to volume contraction.[31] Due to the extra Mn, a much steeper strain reduction is found for $\varphi = 40.0\%$ (black) compared with $\varphi = 33.3\%$ (red) in Figure 4c. During negative scanning, MnO_2 is reduced back to MnOOH at the cathode peak C2, and then continuously reduced to $Mn(OH)_2$ through a wide region from C2 toward the negative potentials.[30a] At the end of the negative scanning (<–1.0 V), hydrogen absorption into Mn metal may occur,[32] which elevates the actuation strain for $\varphi = 40.0\%$ compared with that of $\varphi = 33.3\%$. For further details of recognizing redox peaks in the cyclic voltammograms, a literature survey of reaction potentials of Ni and Mn electrodes working in alkaline solutions is provided in Table S1, Supporting Information.

Figure 4d shows the first derivative of actuation strain to electrode potential. The major differences between the two samples are highlighted by two green rectangles. The right rectangle corresponds to two redox couples of $Mn(OH)_2$/MnOOH and MnOOH/MnO_2, while the left rectangle corresponds to hydrogen absorption/desorption.

During CV, electric charges that pass through the actuators were measured and then plotted against the actuation strain. Figure 4e shows that the actuation strain is proportional to the specific charge during both forward and backward potential scanning. The charge–strain response is around -6×10^{-5} strain per C g^{-1} (linear fit of the curve). The sample that has a higher relative density ($\varphi = 40.0\%$) generates a reversible strain of 1.94%, which is 50% more than the sample with a lower relative density ($\varphi = 33.3\%$). The strain enhancement is due to the electrochemical contributions of Mn. To our knowledge, 1.94% is one of the largest strain amplitudes ever reported in metallic-based electrochemical actuators under a comparable strain rate of 10^{-5} s^{-1}.[16b] It is worth noting that, for nanoporous metals that rely on double-layer charging to induce actuation, the strain amplitude was in the order of 0.1%.[1d,13b] Metals that rely on pseudo-capacitive charging to induce actuation, the strain amplitude was generally around 1.0%;[6,16c] however, strain amplitudes approach to 2% is still difficult to achieve. Bai et al. reported an actuation strain of 2% under square wave potentials in hierarchical structured nanoporous nickel.[16c] For noble metals, Shi et al.[33] and Zhang et al.[34] reported actuation strains of 3.95% and 3.28%, respectively, in nanoporous Pd due to the H absorption/desorption processes and experienced H_2 bubbling.

Following Figure 4b–e, a series of nanoporous Ni–Mn samples were tested by CV and the corresponding strain amplitudes were measured by dilatometry. Figure 4f (left axis) shows a trend that the strain amplitude increases almost linearly with the relative density. As residual Mn is the reason for the increase of relative density, it indicates Mn plays a significant role to enhance the actuation strain amplitude. Figure 4f (right axis) plots the specific capacity of those nanoporous metals as a function of relative density, where the specific capacity was obtained from negative scanning of the CV. It shows the specific capacity is linearly proportional to the relative density, too. Bear in mind the charge-induced strain effect, this explains why the actuation strain amplitude increases with the relative density in Figure 4f (left axis).

In **Figure 5**a–c, electrode potential cyclically scans for 12 successive cycles at a scan rate of 1 mV s^{-1} within the same potential region and electrolyte. Both actuation strain and the corresponding specific charge vary accordingly with potential. As noticed by the arrows, during positive potential scanning, the specific charge increases and the actuation strain decreases; vice versa for the negative potential scanning. These trends are consistent with Figure 4b–d. With relative density increasing from 25.5% to 33.3% and 40.0%, the strain amplitude increases from 0.36% to 1.33% and 1.94% (black, left axis), so as the increase of the charge amplitude from 187 to 251 and 332 C g^{-1} (red, right axis).

For some of the nanoporous Ni–Mn samples, a constant strain shift appears during CV, such as 0.47% strain shift per hour shown in Figure 5c (black curve). It is assumed to represent irreversible passivation of metal surface in alkane electrolyte, such as the formation of a stable β-$Ni(OH)_2$ passive layer on Ni surface that induces irreversible volume expansion.[34] Once the metal surface is fully passivated or stabilized, the strain shift may disappear, such as Figure S8, Supporting Information in ref. [16b], and also Figures 5a, **6**b and Figure S1, Supporting Information in this article. Even though some strain shift happens, the reversible strain amplitudes and the corresponding charge amplitudes remain reversible during successive cycles, as highlighted by the yellow background in Figure 5a–c.

Figure 5d shows a comparison of cyclic voltammograms of three samples with different relative densities. For the sample with a low relative density of 25.5%, the sharp redox peaks of A1/C1 and A3/C3 are very close to those peaks of thin Ni films tested at the same condition, as reported by us before (Figure 1 in ref. [35]), which indicates the negligible influence of Mn species. With relative density increasing to 34.2% and then 41.8%, the residual Mn increases accordingly, as a result, A2/C2 peaks appear and enlarge, which is attributed to the $Mn(OH)_2$ / MnOOH / MnO_2 redox reactions. The A1/C1 peaks also increase with relative density presumably due to the promotion of hydrogen desorption/absorption by extra Mn, as aforementioned in Figure 4 and Table S1, Supporting Information. At a high relative density of $\varphi = 41.8\%$, the actuation strain amplitude approaches to 2%.

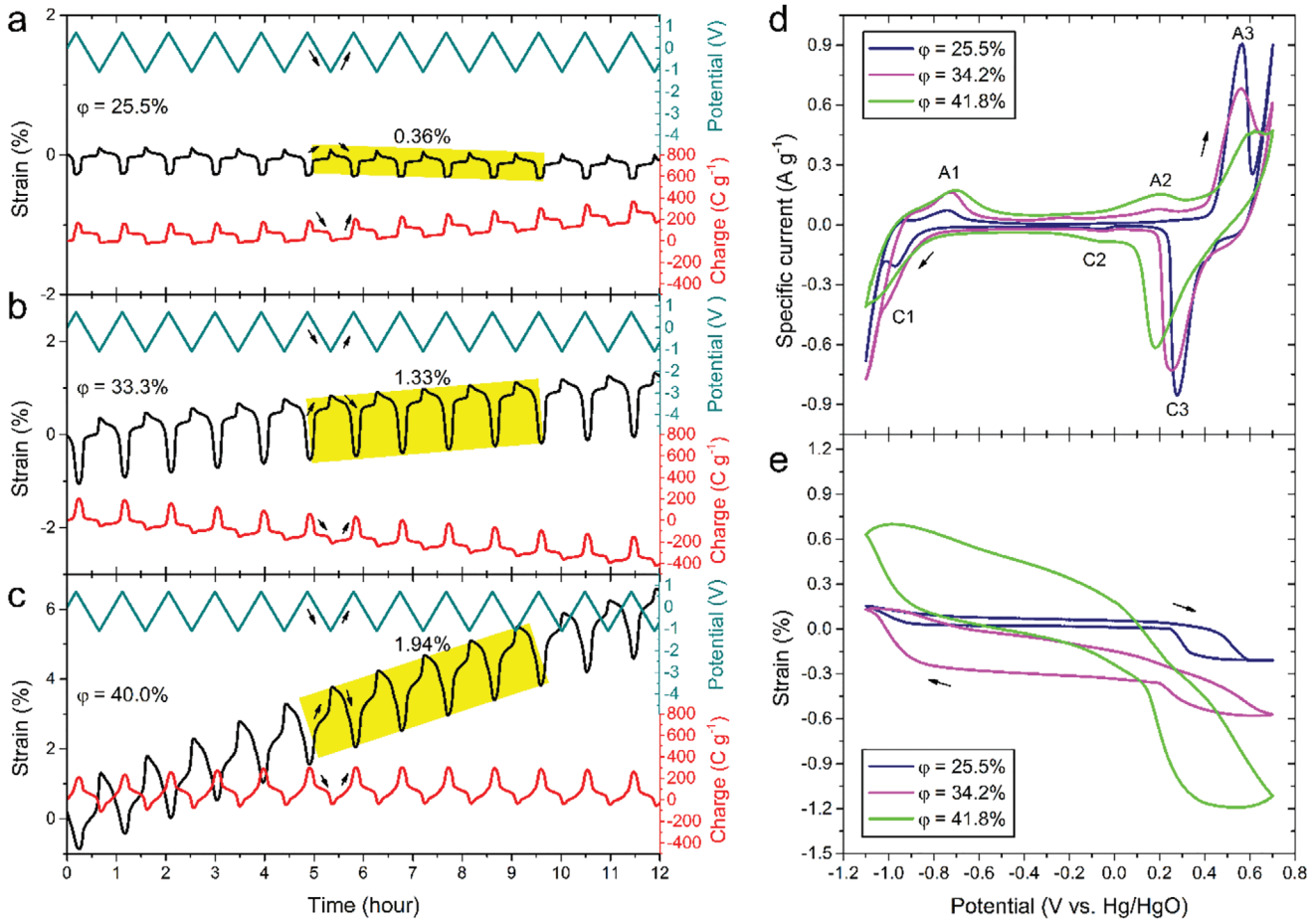

Figure 5. Dependence of electrochemical actuation on relative densities of nanoporous Ni–Mn. a–c) Actuation strain (left axis), specific charge (right axis), and electrode potential (right axis) as a function of actuation time. 12 cycles were scanned in the range of [–1.1, 0.7] V versus Hg/HgO at a rate of 1 mV s^{-1} in 1 M NaOH. d) Specific current as a function of electrode potential and e) the corresponding actuation strain as a function of electrode potential.

For a sample with φ = 32.1%, continuous actuation testing was conducted for ≈5 h without observation of strain shift (Figure S1, Supporting Information). Figure 6a shows that the scan rate decreases from 10 to 5 mV s^{-1}, and to 1 mV s^{-1}, and two cycles are scanned at each scan rate. Accordingly, the actuation strain amplitude increases from 0.53% to 0.74%, and to 1.08% (Figure 6b) and the specific charge amplitude increases from 71 to 113 C g^{-1}, and to 280 C g^{-1} (Figure 6c). After two hours of resting, the strain amplitude is recovered to be 0.52% at 10 mV s^{-1}, which shows a stable and repeatable actuation, as noticed by the dashed lines in Figure 6b,c for curves at 10 mV s^{-1}.

From cyclic voltammograms in Figure 6d, the oxidation peak that close to the positive potential end gradually disappears with the scan rate increasing from 1 to 10 mV s^{-1}, because the sluggish ion transport within the nanoporous structure limits the charge-transfer reaction rate of the redox couples, that is, $Ni(OH)_2$/NiOOH and $Mn(OH)_2$/MnOOH/MnO_2. Accordingly, the actuation strain amplitude decreases most obviously at the corresponding potential range between 0.2 and 0.7 V versus Hg/HgO.

2.3. Relative Density of Nanoporous Ni–Mn

Because actuation strain and specific capacity were measured by separate instruments, that is, a dilatometer and a potentiostat, the consistency between them with respect to relative density undoubtedly proves that the relative density is a key tuning factor to enhance the electrochemical actuation. It is important to have good control of the relative density for actuator design. Therefore, the dependence of relative density on various dealloying conditions was investigated.

After a series of dealloying experiments, four dealloying conditions were found to be the major influencing factors on relative density, that is, dealloying time, acid concentration, dealloying temperature, and precursor mass. Because the $Ni_{30}Mn_{70}$ precursors were cut into a self-similar geometry of ≈1:1:2 dimensional-ratio, the influence of precursors' geometry was not considered here.

When the acid concentration, dealloying temperature, and precursor mass are maintained the same, **Figure 7**a shows that relative density decreases almost linearly with dealloying time. With the precursor mass increasing, the decreasing gradient

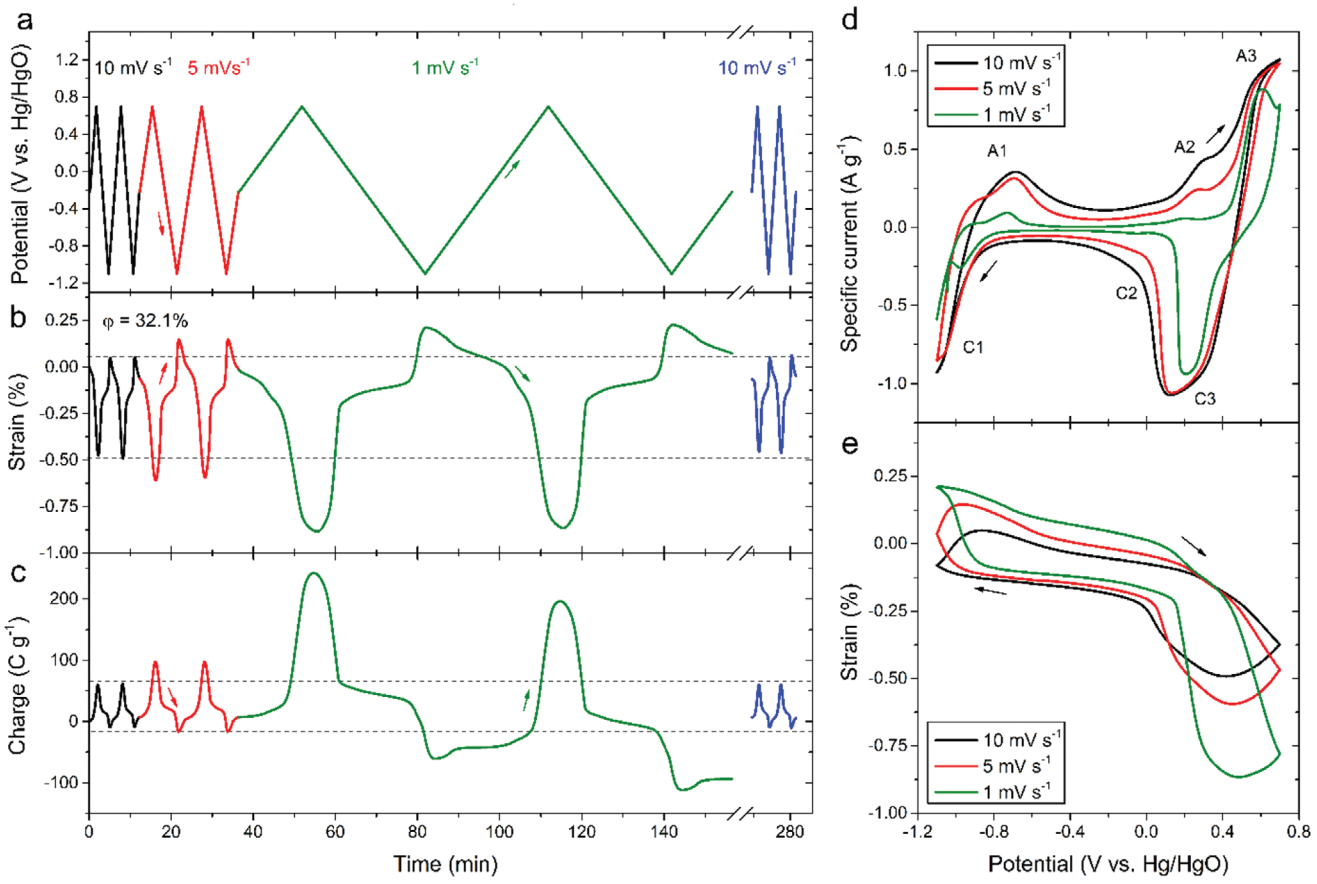

Figure 6. Dependence of electrochemical actuation on potential scan rates. a–c) Electrode potential, actuation strain, and specific charge as a function of actuation time, respectively. The potential scan rate increases from 10, to 5, to 1 mV s^{-1}, and after 2 h of resting, to 10 mV s^{-1} again. Two cycles are scanned at each scan rate. d) Specific current as a function of electrode potential and e) the corresponding actuation strain as a function of electrode potential. The nanoporous Ni–Mn has a relative density of 32.1%.

becomes less steep, because larger samples need more time to be dealloyed to the same extent. As it is not easy to cut mm-sized precursors with identical masses, we use a specific dealloying time (i.e., time divided by precursor mass) to eliminate the influence of mass. Indeed, Figure 7b shows precessors with different masses fall into the same linear relationship between relative density and specific dealloying time. Figure 7c shows that relative density decreases with acid concentration increasing when the other three influencing factors are maintained the same, and Figure 7d shows that relative density decreases with dealloying temperature. Figure 7e summarizes the dependence of relative density on the specific dealloying time at various acid concentrations and temperatures. Remarkably, all the 31 dealloyed samples fall into a simple linear region, as noticed by the grey region in Figure 7e. Therefore, to obtain a nanoporous metal with a certain relative density, even though the dealloying conditions may be different, the required dealloying time can be predicted from Figure 7e. Figure 7f shows that, from SEM-EDX element analysis of the dealloyed samples, the residual Mn content almost linearly increases with the relative density, where residual Mn=Mn at.%/ (Ni at.% +Mn at.%). This relationship correlates the actuation enhancement because of relative density (Figure 4f) to the residual Mn content (Figure 7f).

In Figure S2, Supporting Information, nitrogen adsorption/desorption isotherms analyzed by the density functional theory method reveals that a nanoporous metal with a higher relative density (φ = 41.8%) has a smaller specific surface area (17.5 m^2 g^{-1}), while a sample with a lower relative density (φ = 32.2%) has a larger specific surface area (27.6 m^2 g^{-1}). Thus, the specific surface area of nanoporous metal reduces with residual Mn increasing. It is worth to note that the exact surface area evaluated by different methods may be different, such as double-layer capacitance method[36] and nitrogen adsorption/desorption method,[37] but there it is the relative values that matters for the present discussion. From the pore size distribution shown in Figure S2c, Supporting Information, over 50% of the specific surface area is contributed from pores with radii less than 20 Å (dashed line).

A smaller specific surface area limits the double-layer capacity at the electrode/electrolyte interface, which can lead to the reduction of actuation strain, such as the nanoporous noble metal actuators or nanoporous carbon-based actuators, in which the actuation strain was positively proportional to the specific surface area.[6] It is the case when the actuation mechanism is maintained the same, and the specific surface area becomes the major way to enhance actuation. However, it is not the case when the actuation mechanism changes due to the

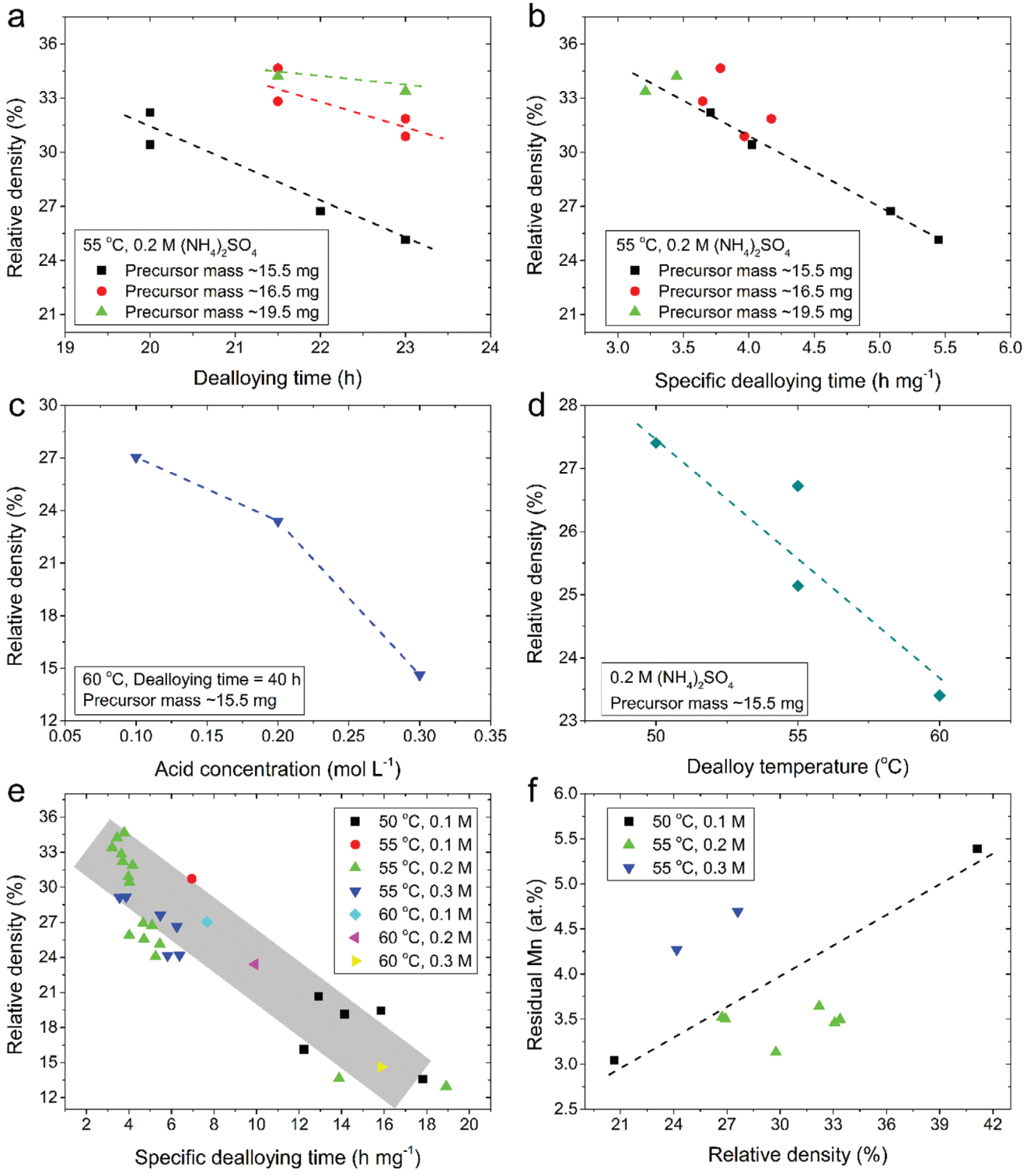

Figure 7. Dependence of relative density on dealloying conditions of as-dealloyed nanoporous metals. a) Relative density versus dealloying time for precursors with different masses. b) Relative density versus specific dealloying time (i.e., normalized dealloying time) corresponding to (a). c) Relative density versus acid concentration of the dealloying solution $(NH_4)_2SO_4$. d) Relative density versus dealloying temperature. e) A statistic plot of relative density as a function of specific dealloying time, at different temperatures and acid concentrations. f) Mn content in the nanoporous Ni–Mn metal as a function of relative density.

adding of a secondary actuation material. A higher relative density corresponds to a lower specific surface area (Figure S2b, Supporting Information), while the higher relative density enhances the actuation strain rather than reduces the strain (Figures 4f, 5a–c). It is because the residual Mn introduces a more effective actuation mechanism than that of the host Ni (Figures 4b, 5d). Therefore, the secondary actuation metal (Mn) within the primary actuation network (Ni) is a solution to avoid the high specific surface area and low relative density in nanoporous metals, while achieving the enhanced actuation strain. As demonstrated in the following section, low relative density is detrimental to the mechanical strength of the nanoporous metals which is another factor for high-performing actuators.

2.4. Mechanical Characterization of Nanoporous Ni–Mn

Besides actuation enhancement, higher relative density brings another benefit for actuator applications, which is the increase of mechanical strength. Uniaxial compression tests of bulk as-dealloyed nanoporous Ni–Mn were conducted. **Figure 8**a shows the engineering stress versus strain relationship. The effective Young's modulus increases (from 421 to 512 MPa) with the unloading strain increasing (from 2% to 5%). This trend is due to the densification of the nanoporous structure under compression.[38] Figure 8b shows the achievable maximum engineering strain increases with the relative density decreasing, but the ultimate engineering strength decreases. The achievable strains are much larger than the charge-induced strain (1.94% in Figure 4b), which means the samples have enough mechanical strength to support the actuation.

Figure 8c shows that the ultimate engineering strength σ_{eng}^{ulti} increases with the relative density and follows an exponential relationship, $\sigma_{eng}^{ulti} = 0.11\exp(0.14\varphi)$, where φ is relative density. This relationship complies with Ryshkewitch–Duchworth model that was obtained from compression tests of porous ceramics.[39] It is different from the well-known Gibson–Ashby formula $\sigma_{eng}^{ulti} = c\sigma_s\varphi^n$, where the best fitting parameters are c = 0.27, n = 2 and σ_s = 450 MPa (the strength of the solid phase). It is possibly because Gibson–Ashby model was derived from idealized porous structures,[18a] which is different from dealloyed porous structures that have a wide range of pore size, disordered arrangement, and dangling ligaments—free end ligaments that do not carry loads.[18b,40] In brief, the extra Mn inside nanoporous Ni–Mn metal not only linearly elevates the actuation strain amplitude (Figure 4f and 7f) but also exponentially enhances the ultimate engineering strength of the actuator (Figure 8c).

3. Conclusion

This article reports a way to simultaneously enhance the actuation strain and mechanical strength of metallic-based electrochemical actuators, which overcomes the critical challenge that hinders the competitive actuation performance. A secondary actuation metal Mn is homogeneously distributed on a 3D interconnected Ni network that is synthesized by chemical dealloying. The actuation amplitude increases with extra Mn

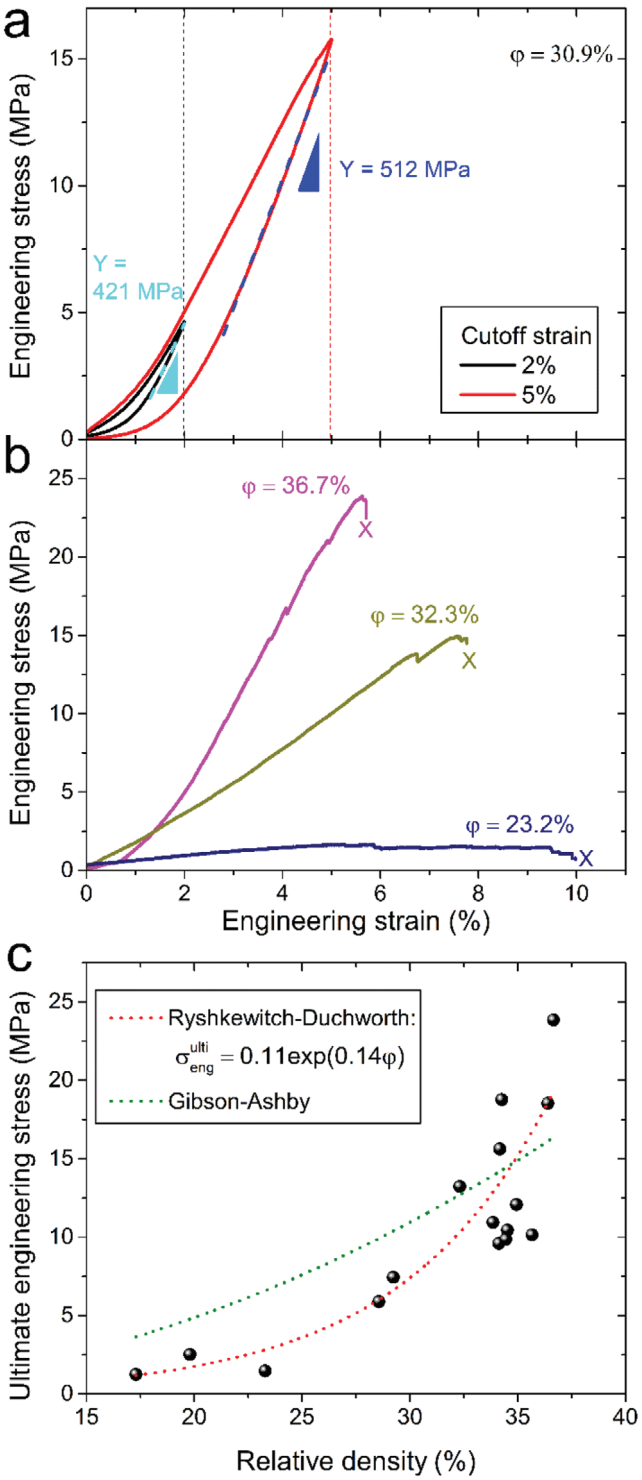

Figure 8. Mechanical characterization of as-dealloyed nanoporous Ni–Mn. a) Engineering stress versus engineering strain for a sample with relative density 30.9%. It is measured by a uniaxial compression test at a 10^{-4} s^{-1} strain rate. Unloading starts at 2% and 5% cutoff-strain, respectively. b) Engineering stress versus engineering strain for samples with different relative densities. c) Ultimate engineering strength as a function of relative density. Symbols are experimental results and dash lines are model fittings.

because of a two-electron-transfer redox of $Mn(OH)_2$/MnOOH/MnO_2, which induces volume expansion/contraction via H^+ intercalation/deintercalation. This actuation mechanism is more effective than the one-electron-transfer redox of $Ni(OH)_2$/NiOOH in the Ni host network. As a result, a strain amplitude of 1.94% is obtained, which is a recorded high value for metallic-based actuators. At the same time, due to the extra Mn content, the mechanical strength of the actuator is enhanced exponentially by the increase of relative density, complying with the Ryshkewitch–Duchworth model. Therefore, this research may find a way to fabricate high actuation performance and mechanically robust metallic actuators.

4. Experimental Section

Synthesis of Nanoporous Ni–Mn Alloy: The synthesis method was reported by the authors before.[16b] $Ni_{30}Mn_{70}$ alloy ingot was cast by an induction cold crucible furnace (Arcast) in Ar atmosphere by using Ni and Mn metals (>99.99% pure, ChemPUR). The ingot was cut into disks (≈16 mm in diameter and ≈2.5 mm in thickness) by a mechanical saw and annealed at 900 °C for 24 h under vacuum and then quenched in water. During heat treatment, the heating rate was not controlled, but the quenching rate was from 900 °C to room temperature within seconds. The disks were mechanically polished and cut into cuboids (≈1 × 1 × 2 mm^3) by diamond wire saw. Bulk nanoporous Ni–Mn was synthesized by chemical dealloying in 0.05, 0.1, 0.2, and 0.3 M $(NH_4)_2SO_4$ solutions at constant temperatures of 70, 50, 55, and 55 °C, respectively. The influence of synthesis conditions on the dealloyed sample is shown in Figure 7.

Materials Characterization: The morphology of nanoporous structures was observed by STEM carried out in an FEI Talos F200X and SEM carried out in a Zeiss Supra 55 VP FEG-SEM combined with EDX. Macroscopic photos of the bulk nanoporous metals were captured by optical microscopy (Leica M205C, Germany). Uniaxial compression tests were conducted on a universal testing machine (Zwick 1474) at a constant engineering strain rate of 10^{-4} s^{-1} with a pre-load of 0.3 N at the beginning of the measurement for close contact between sample and pushrod. The effective (macroscope) Young's modulus was determined during unloading at different deformation stages. The specific surface area of the nanoporous samples was measured by nitrogen adsorption/desorption processes at 77 K using a Quantachrome Autosorb surface analyzer and analyzed by density functional theory method.

Electrochemical Actuation Measurement: The linear actuation strain of bulk nanoporous metal was measured in situ in an electrochemical cell, combined with a computer-controlled dilatometer (Linseis, L75 vertical dilatometer) and a potentiostat (Autolab, PGSTAT302N). A glass push rod which was connected with the displacement sensor of the dilatometer had a constant compressive pressure (≈0.2 MPa) on the top surface of the sample in order to maintain close contact between the pushrod and the sample. The electrochemical cell was filled with 1 M NaOH electrolyte with the nanoporous metal as a WE, a piece of carbon clothes as a counter electrode, and a commercial Hg/HgO reference electrode (Sensortechnik Meinsberg, Germany).

Supporting Information

Supporting Information is available from the Wiley Online Library or from the author.

Acknowledgements

C.C. thank for the Humboldt Research Fellowship from Alexander von Humboldt Foundation, Germany. The authors thank for the financial support of the DFG via SFB "M3" subproject B2. The authors thank Prof. Jörg Weissmüllar for the discussions.

Open access funding enabled and organized by Projekt DEAL.

Conflict of Interest

The authors declare no conflict of interest.

Data Availability Statement

The data that support the findings of this study are available from the corresponding author upon reasonable request.

Keywords

charge-induced strain, dealloying, metallic actuators, nanoporous metals, pesudocapacity

Received: April 13, 2021
Published online: May 13, 2021

[1] a) R. H. Baughman, C. Cui, A. A. Zakhidov, Z. Lqbal, J. N. Barisci, G. M. Spinks, G. G. Wallace, A. Mazzoldi, D. D. Rossi, A. G. Rinzler, O. Jaschinski, S. Roth, M. Kertesz, *Science* **1999**, *284*, 1340; b) M. Acerce, E. K. Akdoğan, M. Chhowalla, *Nature* **2017**, *549*, 370; c) S. Umrao, R. Tabassian, J. Kim, V. H. Nguyen, Q. Zhou, S. Nam, I.-K. Oh, *Sci. Robot.* **2019**, *4*, eaaw7797; d) J. Weissmüller, R. N. Viswanath, D. Kramer, P. Zimmer, R. Würschum, H. Gleiter, *Science* **2003**, *300*, 312.

[2] a) Q. M. Zhang, H. F. Li, M. Poh, F. Xia, Z. Y. Cheng, H. S. Xu, C. Huang, *Nature* **2002**, *419*, 284; b) Q. Zhang, V. Bharti, X. Zhao, *Science* **1998**, *280*, 2101; c) I. Kim, H. Roh, J. Yu, N. Jayababu, D. Kim, *ACS Energy Lett.* **2020**, *5*, 1577; d) R. H. Baughman, *Science* **2003**, *300*, 268; e) C. Lu, Y. Yang, J. Wang, R. Fu, X. Zhao, L. Zhao, Y. Ming, Y. Hu, H. Lin, X. Tao, Y. Li, W. Chen, *Nat. Commun.* **2018**, *9*, 752.

[3] J. Mu, M. Jung de Andrade, S. Fang, X. Wang, E. Gao, N. Li, S. H. Kim, H. Wang, C. Hou, Q. Zhang, M. Zhu, D. Qian, H. Lu, D. Kongahage, S. Talebian, J. Foroughi, G. Spinks, H. Kim, T. H. Ware, H. J. Sim, D. Y. Lee, Y. Jang, S. J. Kim, R. H. Baughman, *Science* **2019**, *365*, 150.

[4] E. W. H. Jager, O. Inganas, I. Lundström, *Science* **2000**, *288*, 2335.

[5] K. W. Kwan, S. J. Li, N. Y. Hau, W.-D. Li, S. P. Feng, A. H. W. Ngan, *Sci. Robot.* **2018**, *3*, eaat4051.

[6] H. J. Jin, X. L. Wang, S. Parida, K. Wang, M. Seo, J. Weissmüller, *Nano Lett.* **2010**, *10*, 187.

[7] a) C. Cheng, J. Weissmüller, A. H. W. Ngan, *Adv. Mater.* **2016**, *28*, 5315; b) D. Kramer, R. N. Viswanath, J. Weissmüller, *Nano Lett.* **2004**, *4*, 793.

[8] a) Z. Jiao, C. Zhang, W. Wang, M. Pan, H. Yang, J. Zou, *Adv. Sci.* **2019**, *6*, 1901371; b) H. Chu, X. Hu, Z. Wang, J. Mu, N. Li, X. Zhou, S. Fang, C. S. Haines, J. W. Park, S. Qin, N. Yuan, J. Xu, S. Tawfick, H. Kim, P. Conlin, M. Cho, K. Cho, J. Oh, S. Nielsen, K. A. Alberto, J. M. Razal, J. Foroughi, G. M. Spinks, S. J. Kim, J. Ding, J. Leng, R. H. Baughman, *Science* **2021**, *371*, 494.

[9] a) M. Hughes, G. M. Spinks, *Adv. Mater.* **2005**, *17*, 443; b) T. Zheng, P. Pour Shahid Saeed Abadi, J. Seo, B.-H. Cha, B. Miccoli, Y.-C. Li, K. Park, S. Park, S.-J. Choi, R. Bayaniahangar, D. Zhang, S.-H. Lee, C.-K. Lee, A. Khademhosseini, S. R. Shin, *ACS Appl. Mater. Interfaces* **2019**, *11*, 20615; c) G. W. Rogers, J. Z. Liu, *J. Am. Chem. Soc.* **2011**, *133*, 10858.

[10] a) T. H. T. Fook, J. H. Jeon, P. S. Lee, *Adv. Mater. Technol.* **2020**, *5*, 1900762; b) J. G. Martinez, T. F. Otero, E. W. H. Jager, *Langmuir* **2014**, *30*, 3894.
[11] a) Y. Yan, T. Santaniello, L. G. Bettini, C. Minnai, A. Bellacicca, R. Porotti, I. Denti, G. Faraone, M. Merlini, C. Lenardi, P. Milani, *Adv. Mater.* **2017**, *29*, 1606109; b) Q. He, Z. Liu, G. Yin, Y. Yue, M. Yu, H. Li, K. Ji, X. Xu, Z. Dai, M. Chen, *Smart Mater. Struct.* **2020**, *29*, 045013; c) E. Griffiths, J. Wilmers, S. Bargmann, B. D. Reddy, *J. Mech. Phys. Solids* **2020**, *137*, 103848.
[12] a) E. Detsi, S. H. Tolbert, S. Punzhin, J. T. M. De Hosson, *J. Mater. Sci.* **2016**, *51*, 615; b) E. Detsi, P. Onck, J. T. M. De Hosson, *ACS Nano* **2013**, *7*, 4299; c) T. Juarez, J. Biener, J. Weissmüller, A. M. Hodge, *Adv. Eng. Mater.* **2017**, *19*, 1700389.
[13] a) Y. H. Xue, J. Markmann, H. L. Duan, J. Weissmüller, P. Huber, *Nat. Commun.* **2014**, *5*, 4237; b) H. J. Jin, J. Weissmüller, *Science* **2011**, *332*, 1179; c) Q. Bai, C. Zhang, F. Tan, F. Wu, Z. Zhang, *Electrochem. Commun.* **2021**, *124*, 106940; d) R. N. Viswanath, D. Kramer, J. Weissmüller, *Electrochim. Acta* **2008**, *53*, 2757.
[14] Z. Qi, J. Weissmüller, *ACS Nano* **2013**, *7*, 5948.
[15] X. L. Ye, H. J. Jin, *Appl. Phys. Lett.* **2013**, *103*, 201912.
[16] a) M. Hakamada, S. Matsumura, M. Mabuchi, *Mater. Lett.* **2012**, *70*, 132; b) C. Cheng, L. Lührs, T. Krekeler, M. Ritter, J. Weissmüller, *Nano Lett.* **2017**, *17*, 4774; c) Q. Bai, Y. Wang, J. Zhang, Y. Ding, Z. Peng, Z. Zhang, *J. Mater. Chem. C* **2016**, *4*, 45; d) C. Cheng, A. H. W. Ngan, *ACS Nano* **2015**, *9*, 3984.
[17] B. E. Conway, *Electrochemical Supercapacitors: Scientific Fundamentals and Technological Applications*, Springer Science & Business Media, New York **2013**.
[18] a) L. J. Gibson, M. F. Ashby, *Cellular Solids: Structure and Properties*, Cambridge University Press, Cambridge **1997**; b) Y.-H. Xiang, L.-Z. Liu, J.-C. Shao, H.-J. Jin, *Acta. Mater.* **2020**, *186*, 105.
[19] J. Erlebacher, M. J. Aziz, A. Karma, N. Dimitrov, K. Sieradzki, *Nature* **2001**, *410*, 450.
[20] a) M. Toupin, T. Brousse, D. Bélanger, *Chem. Mater.* **2004**, *16*, 3184; b) J. L. Kang, A. Hirata, H. J. Qiu, L. Y. Chen, X. B. Ge, T. Fujita, M. W. Chen, *Adv. Mater.* **2014**, *26*, 269; c) X. Lang, A. Hirata, T. Fujita, M. Chen, *Nat. Nanotechnol.* **2011**, *6*, 232.
[21] a) L. Liu, L. Su, Y. Lu, Q. Zhang, L. Zhang, S. Lei, S. Shi, M. D. Levi, X. Yan, *Adv. Funct. Mater.* **2019**, *29*, 1806778; b) Z. M. Chan, D. A. Kitchaev, J. N. Weker, C. Schnedermann, K. Lim, G. Ceder, W. Tumas, M. F. Toney, D. G. Nocera, *Proc. Natl. Acad. Sci. USA* **2018**, *115*, E5261.
[22] J. Weissmüller, K. Sieradzki, *MRS Bull.* **2018**, *43*, 14.
[23] D. B. Williams, C. B. Carter, *Transmission Electron Microscopy, Part 1: Basics*, Springer, New York **2009**.
[24] A. Biswal, B. C. Tripathy, K. Sanjay, T. Subbaiah, M. Minakshi, *RSC Adv.* **2015**, *5*, 58255.
[25] a) D. S. Hall, C. Bock, B. R. MacDougall, *J. Electrochem. Soc.* **2013**, *160*, F235; b) B. Baranowski, S. Majchrzak, T. B. Flanagan, *J. Phys. F: Met. Phys.* **1971**, *1*, 258; c) D. S. Hall, D. J. Lockwood, C. Bock, B. R. MacDougall, *Proc. R. Soc. A* **2015**, *471*, 20140792.
[26] S. L. Yau, F. R. F. Fan, T. P. Moffat, A. J. Bard, *J. Phys. Chem.* **1994**, *98*, 5493.
[27] a) D. Singh, *J. Electrochem. Soc.* **1998**, *145*, 116; b) M. B. J. G. Freitas, *J. Power Sources* **2001**, *93*, 163; c) M. S. Kim, K. B. Kim, *J. Electrochem. Soc.* **1998**, *145*, 507; d) M. S. Kim, T. S. Hwang, K. B. Kim, *J. Electrochem. Soc.* **1997**, *144*, 1537.
[28] a) M. Pourbaix, *Atlas of Electrochemical Equilibria in Aqueous Solutions*, Pergamon Press Ltd., London **1966**; b) A. J. Bard, R. Parsons, J. Jordan, *Standard Potentials in Aqueous Solutions*, Marcel Dekker, Inc., New York **1985**.
[29] D. K. Cha, *J. Electrochem. Soc.* **1997**, *144*, 2573.
[30] a) A. Kozawa, J. F. Yeager, *J. Electrochem. Soc.* **1965**, *112*, 959; b) J. Haines, J. M. Léger, S. Hoyau, *J. Phys. Chem. Solids* **1995**, *56*, 965; c) W. M. Dose, J. Lehr, S. W. Donne, *Mater. Res. Bull.* **2012**, *47*, 1827.
[31] a) D. A. Kitchaev, S. T. Dacek, W. H. Sun, G. Ceder, *J. Am. Chem. Soc.* **2017**, *139*, 2672; b) C. Poinsignon, M. Amarilla, F. Tedjar, *J. Mater. Chem.* **1993**, *3*, 1227.
[32] M. Krukowski, B. Baranowski, *J. Less-Common Met.* **1976**, *49*, 385.
[33] S. Shi, J. Markmann, J. Weissmüller, *Philos. Mag* **2017**, *97*, 1571.
[34] D. S. Hall, *Ph.D. Thesis*, University of Ottawa, Canada **2014**.
[35] C. Cheng, P. S. Grant, L. Lührs, *Adv. Electron. Mater.* **2020**, *6*, 1900364.
[36] C. Lakshmanan, R. N. Viswanath, S. R. Polaki, R. Rajaraman, *AIP Conf. Proc.* **2015**, *1665*, 140033.
[37] H. J. Qiu, Y. Ito, M. W. Chen, *Scr. Mater.* **2014**, *89*, 69.
[38] N. Mameka, J. Markmann, H. J. Jin, J. Weissmüller, *Acta Mater.* **2014**, *76*, 272.
[39] a) E. Ryshkewitch, *J. Am. Ceram. Soc.* **1953**, *36*, 65; b) S. C. Carniglia, *J. Am. Ceram. Soc.* **1972**, *55*, 610.
[40] N. Huber, R. N. Viswanath, N. Mameka, J. Markmann, J. Weissmüller, *Acta Mater.* **2014**, *67*, 252.